Poly ADP-Ribose Signaling is Dysregulated in Huntington's Disease Patients

Tamara Maiuri (0000-0002-6103-5835)*[1], Carlos Barba Bazan (0000-0002-1884-5760)[1], Rachel J. Harding (0000-0002-1134-391X)[2], Nola Begeja (0000-0002-9805-8037)[1], Tae-In Kam (0000-0002-7241-4902)[3,4], Lauren M. Byrne (0000-0003-1650-4273)[5], Filipe B. Rodrigues (0000-0002-5567-7938)[5], Monica M. Warner (0000-0002-7677-127X)[1, 6], Kaitlyn Neuman (0000-0001-7699-9680)[1], Muqtasid Mansoor (0000-0001-8192-6590)[1], Mohsen Badiee (0000-0003-3722-4609)[7], Morgan Dasovich (0001-0000-7951-9662)[7], Anthony K. L. Leung (0000-0001-5569-4036)[7,8], Sara N. Andres (0000-0002-4795-2856)[1,6], Edward J. Wild (0000-0002-6921-7887)[5], Ted M. Dawson (0000-0002-6459-0893)[3,4,9,10], Valina L. Dawson (0000-0002-2915-3970)[3,4,9a,10], Cheryl H. Arrowsmith (0000-0002-4971-3250)[2,11], and Ray Truant (0000-0003-2542-6641)*[1]

[1]Department of Biochemistry and Biomedical Sciences, McMaster University, Hamilton, Canada
[2]Structural Genomics Consortium, University of Toronto, Toronto, Canada
[3]Neurodegeneration and Stem Cell Programs, Institute for Cell Engineering, Johns Hopkins University School of Medicine, Baltimore, MD 21205, USA
[4]Department of Neurology, Johns Hopkins University School of Medicine, Baltimore, MD 21205, USA
[5]UCL Huntington's Disease Centre, UCL Queen Square Institute of Neurology, University College London, London, UK
[6]Michael G. DeGroote Institute for Infectious Disease Research, McMaster University, Hamilton, ON, Canada
[7]Department of Biochemistry and Molecular Biology, Bloomberg School of Public Health, Johns Hopkins University, Baltimore, MD, USA
[8]Department of Molecular Biology and Genetics, Department of Genetic Medicine, Department of Oncology, School of Medicine, Johns Hopkins University, Baltimore, MD, USA
[9]Department of Pharmacology and Molecular Sciences, Johns Hopkins University School of Medicine, Baltimore, MD 21205, USA
[9a]Department of Physiology, Johns Hopkins University School of Medicine, Baltimore, MD 21205, USA
[10]Solomon H. Snyder Department of Neuroscience, Johns Hopkins University School of Medicine, Baltimore, MD 21205, USA
[11]University Health Network, Toronto, Canada

*Corresponding authors: maiurit@mcmaster.ca, truantr@mcmaster.ca

Abstract

Huntington's disease (HD) is an autosomal dominant genetic neurodegenerative disease caused by a CAG expansion in the *Huntingtin (HTT)* gene, translating to an expanded polyglutamine tract in the huntingtin (HTT) protein. Age at disease onset is correlated to CAG repeat length, but varies by decades between individuals with identical repeat lengths. Genome-wide association studies link HD modification to DNA repair and mitochondrial health pathways. Recent clinical studies show elevated DNA damage in HD, even at the premanifest stage of disease. One of the major DNA repair nodes influencing neurodegenerative disease is the PARP pathway. Accumulation of poly ADP-ribose (PAR), produced by PARP1 and PARP2, has been implicated in the pathology of Alzheimer's and Parkinson's diseases, as well as autosomal recessive cerebellar ataxia. We report that HD mutation carriers have lower cerebrospinal fluid PAR levels than healthy controls, starting at the premanifest stage. Patient-derived fibroblasts have reduced PARP1/2 activity and elevated DNA damage, while elevated PAR levels are only revealed upon inhibition of PAR degradation. These phenotypes are rescued by moderate huntingtin level reduction via the huntingtin-lowering splice modulator drug, LMI070 (Branaplam). As a direct mechanism, we have defined a PAR-binding motif in huntingtin, detected huntingtin complexed with PARylated proteins in human cells during stress, and localized huntingtin to mitotic chromosomes upon inhibition of PAR degradation. Direct huntingtin PAR binding was measured by fluorescence polarization and visualized by atomic force microscopy. These results provide insight into a very early molecular mechanism of HD, suggesting possible targets in HD to design early preventive therapies.

Introduction

Huntington's disease (HD) is an autosomal dominant genetic neurodegenerative disease caused by a CAG expansion in exon1 of the *Huntingtin (HTT)* gene, which translates to an expanded polyglutamine tract in the huntingtin (HTT) protein. HD is characterized by psychiatric, cognitive, and motor disturbances for which some symptom management treatments exist, but the search continues for disease-modifying therapies. Age at disease onset is negatively correlated with CAG expansion length, and onset typically occurs in the third or fourth decades of life [1]. However, age at disease onset in individuals with the same CAG length can vary by decades [2,3]. This variability has an inherited component [4,5], suggesting that other genes may act as modifiers of disease onset. Genome-wide association studies (GWAS) have primarily implicated DNA repair and maintenance pathways as such modifiers [2,3,6,7]. While the pathogenic mechanisms have yet to be elucidated, single nucleotide polymorphisms in DNA repair genes that affect somatic instability of the huntingtin locus have been linked to age at onset [8–10], and elevated levels of DNA damage in HD models and tissues have been reported [11–18].

The connection between DNA repair and neurodegeneration is not unique to Huntington's disease, and has been described for Alzheimer's disease [19], Parkinson's disease [20], spinocerebellar ataxias [21,22], and amyotrophic lateral sclerosis [23]. Inherited mutations in a number of DNA repair genes cause neurodegenerative disorders [24–28], and of the nine neurodegenerative genetic polyglutamine diseases, seven of the causative proteins have been implicated in the DNA damage response [29]. Huntingtin forms a transcription-coupled DNA repair complex with RNA polymerase II subunit A, PNKP, and ataxin-3, and mutant huntingtin interferes with this function [30,31]. We have previously reported that huntingtin interacts with ATM, and that ATM kinase activity is required for huntingtin-chromatin interaction in response to oxidative stress [12]. We have more recently identified a similar relationship between ATM and ataxin-1, the protein product of the *ATXN1* gene mutated in spinocerebellar ataxia 1 [32]. ATM signaling is also dysregulated in HD models and brain tissue [11], placing it as a major DNA damage repair node in neurodegenerative diseases.

Another such major node of DNA damage repair is PARP signaling, which has been implicated in Alzheimer's, Parkinson's, and Huntington's diseases (reviewed in [33]) as well as progressive cerebellar ataxia [27]. Of the 17 members of the PARP family, PARP1 and PARP2 play the biggest role in the DNA damage response, with PARP1 accounting for 80-90% of DNA repair-related activity [34,35]. Upon activation by DNA breaks, PARP1 and PARP2 use ADP-ribose units from nicotinamide adenine dinucleotide (NAD^+) as building blocks to generate poly ADP-ribose (PAR) chains of varying length and branching structure. PAR chains act as recruitment scaffolds for DNA repair proteins [36–38]. Part of the repair process involves PAR degradation by poly ADP-ribose glycohydrolase (PARG), which is required to allow DNA repair proteins access to the damaged DNA [39], and to recycle ATP precursor metabolites [40,41].

Excessive PAR polymerization results in NAD^+ depletion, energy crisis, and cell death by necrosis [42]. PAR can also trigger the non-apoptotic programmed cell death termed parthanatos [43], which is particularly important in neurodegenerative disease [44]. Hyper-PARylation has been implicated in several neurodegenerative diseases [27,45–47], including HD [48–50].

Here, we show that PAR signaling is dysregulated in HD patient cells and cerebrospinal fluid (CSF). Analysis of HD mutation carrier CSF samples revealed lower total PAR levels than control samples, a difference evident from the premainfest stage. The activity of PARP1/2 was reduced in fibroblasts from HD patients compared to control fibroblast lines. Despite this, elevated PAR levels in HD fibroblasts were detectable upon inhibition of PARG, consistent with the elevated DNA damage observed in these cells. This phenotype was rescued by the huntingtin-lowering splice modulator drug, LMI070 (Branaplam). We detected huntingtin complexed with PARylated proteins in human retinal epithelial cells, which prompted analysis of the huntingtin structure and identification of a PAR-binding motif. Fluorescence polarization and atomic force microscopy revealed a direct interaction between huntingtin protein and PAR polymers, providing a possible mechanistic link to the observations made in patient cells and CSF. These results provide insight into the very early molecular mechanism of HD pathogenesis, to potentially reveal targets for an early prevention therapy for HD.

Results

The PAR response is deficient in HD patient-derived samples

Elevated PAR levels have been observed in human samples from multiple neurodegenerative diseases [27,45–47]. Although PARP1 inhibition was reported to be neuroprotective in a mouse model of HD [48,49], and elevated PARP1 levels were observed in the neurons and glia of the caudate nucleus from HD patients [50], it remains unknown whether hyper-PARylation contributes to HD pathology. As cancer drugs targeting PARP1 are under consideration for repurposing to treat neurodegenerative diseases [51,52], investigation of their potential for HD is imperative.

We and others have previously reported elevated levels of DNA damage in fibroblasts derived from HD patients compared to controls [12,53,54]. As measured by comet assay, this phenotype was evident under conditions of oxidative stress, but not under basal conditions [12]. To determine whether basal DNA damage levels are elevated in hTERT-immortalized patient-derived fibroblasts, TruHD cells [55], we employed STRIDE, a more sensitive assay for detecting single- and double-strand DNA breaks [56]. We found an increased number of double-strand, but not single-strand breaks, in the nuclei of HD patient cells (TruHD-Q43Q17) compared to controls (TruHD-Q21Q18) (**Fig 1A**).

In response to double-strand DNA damage, PARP1 accumulates at break sites and generates PAR [57–59]. We therefore aimed to determine whether the observed increase in double-strand breaks was reflected by elevated PAR levels in the context of the HD mutation. As shown in **Fig 1B**, we found no corresponding increase in PAR levels under basal conditions in HD fibroblasts, despite the higher level of DSBs. We further measured PAR levels in response to oxidative stress, to test whether the elevated DNA damage phenotype that we previously measured by comet assay [12] is reflected by an elevated PAR phenotype, and found no difference between control and HD patient-derived cells (**Fig 1B**).

To test a patient-relevant CNS-specific tissue, we next measured PAR levels in CSF from HD patients compared to controls. Samples were obtained from the HD-CSF study, an 80-participant cross-sectional study of HD mutation carriers and matched healthy controls [60,61]. Unlike similar

analyses in Parkinson's disease [47], we found that PAR levels were significantly lower in the CSF from both pre-manifest ($p = 0.0001$) and manifest HD patients ($p = 0.0004$) compared to controls, and that disease stage had a large effect on PAR levels in CSF ($\eta^2_p = 0.35$) (**Fig 1C**). PAR levels in the CSF of HD mutation carriers did not correlate with CSF mutant huntingtin or neurofilament light chain (NfL) levels, both of which were shown to correlate with disease severity in HD patients [60,61] (**Fig S1**). In addition, CSF PAR levels in HD mutation carriers did not correlate with clinical measures of disease progression such as disease burden score, total functional capacity, or total motor score (**Fig S2**). Together, the reduced PAR levels in HD patient CSF, and lack of elevated PAR in the context of elevated DNA damage in patient-derived cells, suggest that the PAR response may be deficient in HD patients.

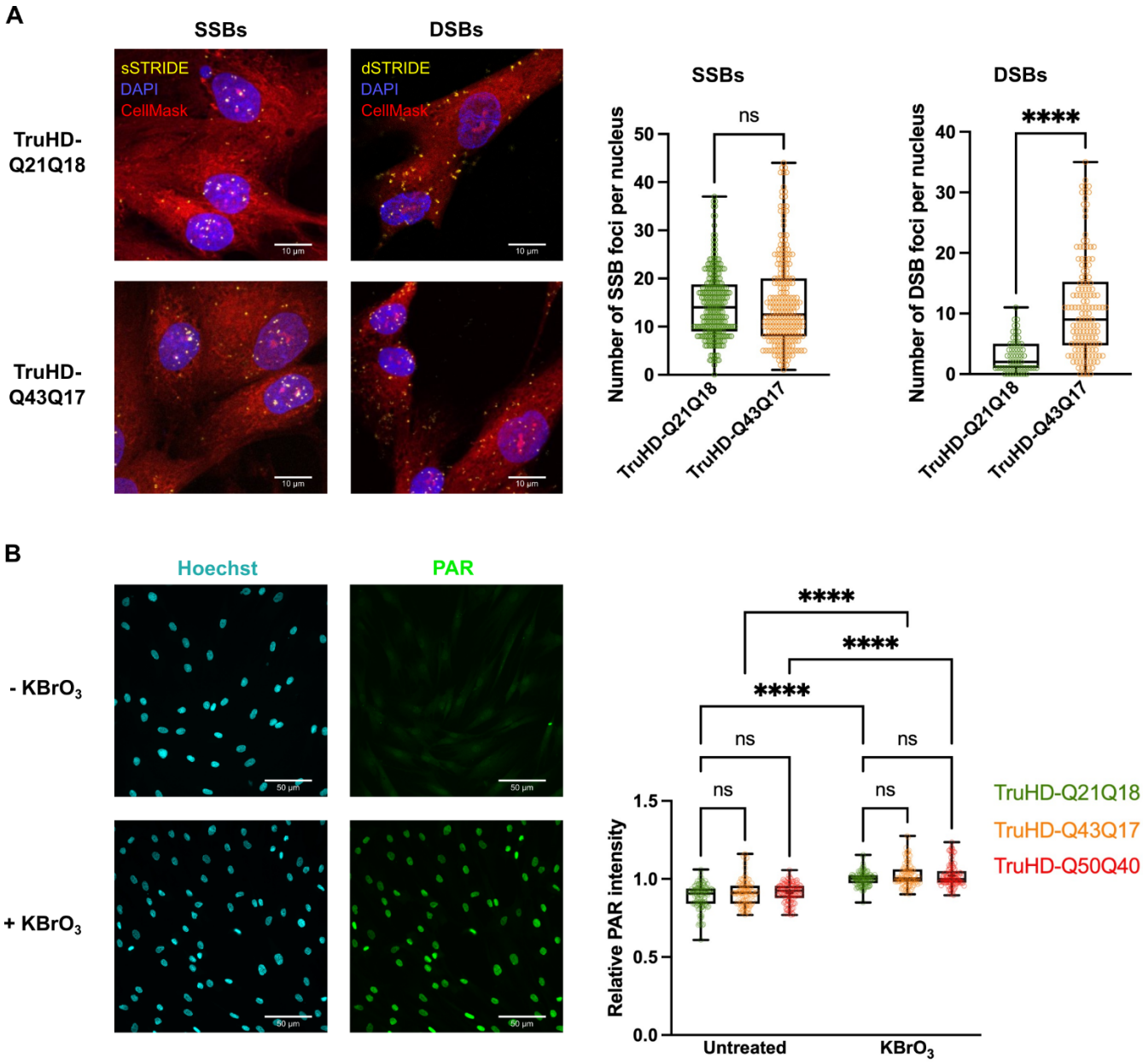
A
SSBs
DSBs
sSTRIDE
DAPI
CellMask
dSTRIDE
DAPI
CellMask
TruHD-Q21Q18
TruHD-Q43Q17
10 µm
SSBs
DSBs
ns
****
Number of SSB foci per nucleus
Number of DSB foci per nucleus
TruHD-Q21Q18
TruHD-Q43Q17
B
Hoechst
PAR
- KBrO3
+ KBrO3
50 µm
****
****
****
ns
ns
ns
ns
Relative PAR intensity
Untreated
KBrO3
TruHD-Q21Q18
TruHD-Q43Q17
TruHD-Q50Q40
C
p = 0.0004*
p = 0.0001*
PAR (log pM)
Controls
Premanifest HD
Manifest HD

Figure 1: The PAR response is deficient in HD patient-derived samples
A: hTERT-immortalized control (TruHD-Q21Q18) and HD patient (TruHD-Q43Q17) fibroblasts were analyzed by STRIDE labeling of single- (SSB) and double-strand (DSB) breaks as described in methods. Representative images are shown (left). Each data point represents the value for a single nucleus (right). Outliers were identified by ROUT method (Q = 1%) and removed. Values were analyzed by Mann-Whitney test (****p<0.0001). **B**: TruHD cells were treated with 100 mM $KBrO_3$ for 30 min followed by fixation and staining with MABE1031 PAR detection reagent. Representative images of TruHD-Q21Q18 cells are shown. Nuclear PAR intensity was measured using CellProfiler, mean intensity recorded for each image (12 images per condition; >1000 cells), and values normalized to the control $KBrO_3$ response condition. Data from nine experiments is shown. Results were analyzed by two-way ANOVA and corrected for multiple comparisons using Tukey's test. **C**: CSF samples from control (n=17), premanifest HD (n=35), and manifest HD (n=19) subjects were blinded and analyzed for PAR levels by ELISA. Group comparisons were assessed using multiple regression with post-hoc Wald tests. *Survives Bonferroni correction for multiple comparisons.

PAR dysregulation is rescued by huntingtin knockdown

We next examined the mechanisms of PAR production and degradation in TruHD cells. By inhibiting PARG, a protein that reverses the actions of PARP enzymes, we were able to induce elevated PAR levels in HD patient-derived fibroblasts compared to controls (**Fig 2A**), consistent with the higher DNA damage levels we detected in these cells (**Fig 1A** and [12]). Thus, the elevated PAR phenotype we would expect in HD cells bearing more DNA damage can be detected only upon inhibition of PAR degradation (**Fig 2A** vs. **Fig 1B**). To determine whether the lower than expected PAR levels were due to increased PARG activity, we performed dose response experiments to measure PARG inhibitor PDD00017273 EC_{50} [62] and found no difference between HD and control cells (**Fig 2B**). In contrast, dose response experiments to calculate the PARP1/2 inhibitor veliparib IC_{50} in TruHD cells revealed lower PARP1/2 activity in HD cells compared to controls (TruHD-Q21Q18 IC_{50} = 140 nM; TruHD-Q43Q17 IC_{50} = 60 nM; TruHD-Q50Q40 IC_{50} = 60 nM) (**Fig 2B**). This is despite similar levels of PARP1, PARP2, and PARG across cell lines (**Fig S3A**) and equal PARP1 chromatin retention upon oxidative stress (**Fig S3B**). Thus, HD cells have reduced PARP1/2 activity and elevated DNA damage, with a concomitant hyper-PAR phenotype that can only be observed upon inhibition of PAR turnover.

To determine whether the huntingtin protein is responsible for the PARG inhibitor-dependent hyper-PAR phenotype in HD cells, we employed LMI070, a small molecule splicing modulator that reduces huntingtin levels [63,64]. We found that LMI070 treatment effecting a 30% reduction in total huntingtin protein levels (**Fig S4**) restored the PAR response in HD cells to that of control cells (**Fig 2C**).

LMI070 treatment also partially rescued the elevated γ-H2AX levels observed in HD cells (**Fig 2D**). Although LMI070 has other targets [64], it had no effect on the PAR response in control cells (**Fig 2C**). This suggests that the elevated PAR levels in HD cells are associated with the presence of mutant huntingtin, and that modest knockdown of huntingtin can rescue PAR dysregulation in HD cells.

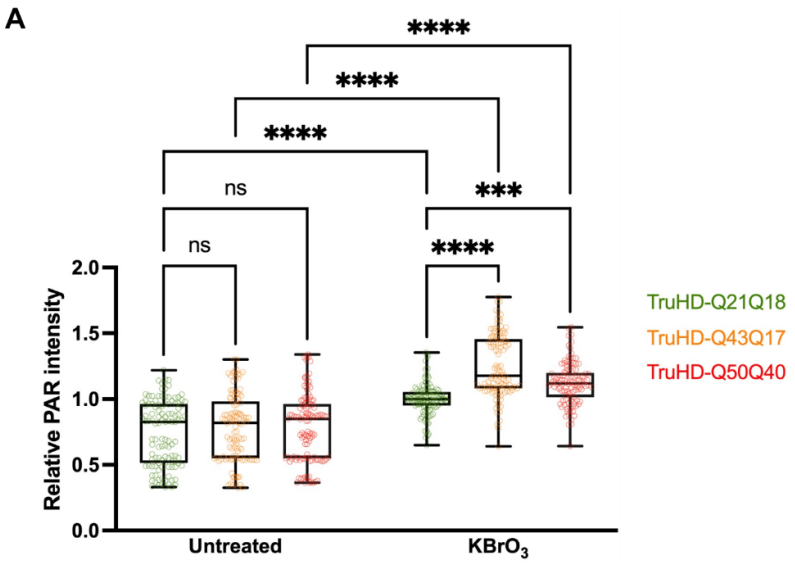
A
****
****
****
ns
***
ns
****
Relative PAR intensity
2.0
1.5
1.0
0.5
0.0
Untreated
KBrO3
TruHD-Q21Q18
TruHD-Q43Q17
TruHD-Q50Q40

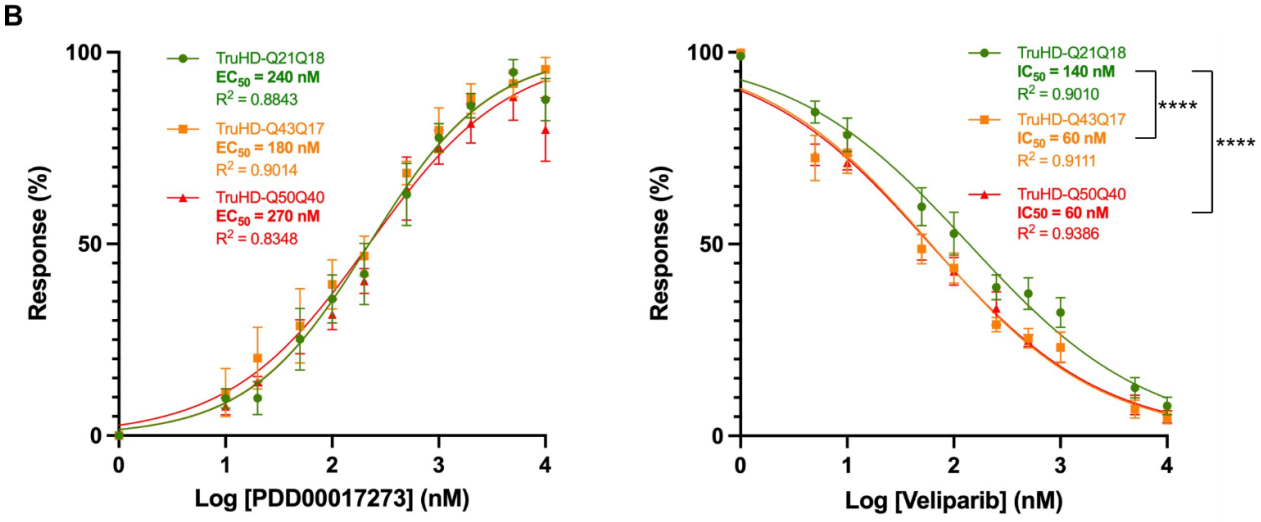
B
TruHD-Q21Q18
EC50 = 240 nM
R2 = 0.8843
TruHD-Q43Q17
EC50 = 180 nM
R2 = 0.9014
TruHD-Q50Q40
EC50 = 270 nM
R2 = 0.8348
Response (%)
Log [PDD00017273] (nM)
TruHD-Q21Q18
IC50 = 140 nM
R2 = 0.9010
TruHD-Q43Q17
IC50 = 60 nM
R2 = 0.9111
TruHD-Q50Q40
IC50 = 60 nM
R2 = 0.9386
****
****
Response (%)
Log [Veliparib] (nM)

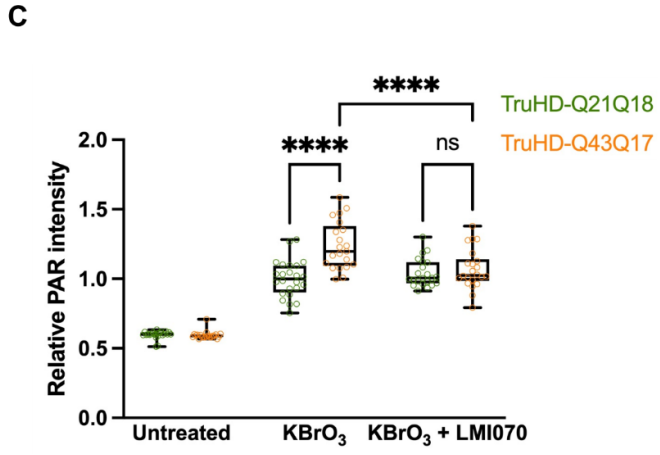
C
****
****
ns
TruHD-Q21Q18
TruHD-Q43Q17
Relative PAR intensity
Untreated
KBrO3
KBrO3 + LMI070

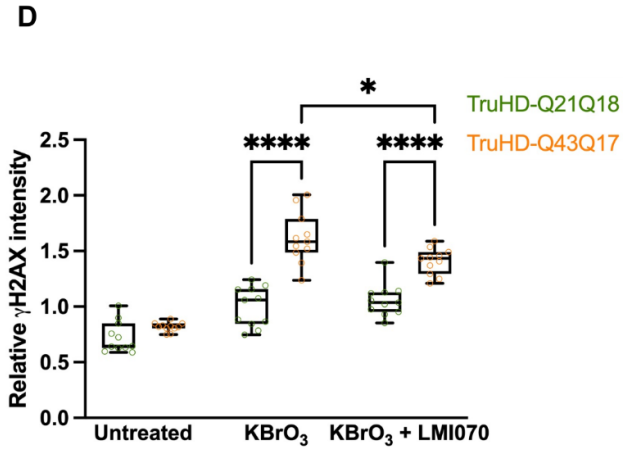
D
*
****
****
TruHD-Q21Q18
TruHD-Q43Q17
Relative γH2AX intensity
Untreated
KBrO3
KBrO3 + LMI070

Figure 2: PAR dysregulation is rescued by huntingtin lowering
A: TruHD cells were pre-treated with 10 μM PARG inhibitor PDD00017273 for 30 min followed by 100 mM $KBrO_3$ for 30 min in the presence of PARG inhibitor and analyzed as in Figure 1B. Data from nine experiments is shown (***p<0.001; ****p<0.0001). **B**: Fibroblasts were pre-treated with increasing doses of PDD00017273 (left) or veliparib (right) for 30 min followed by 100 mM $KBrO_3$ for 30 min in the presence of inhibitor. Veliparib dose response was carried out in the presence of 10 μM PARG inhibitor to enable pan-ADP-ribose detection by MABE1016. EC_{50} and IC_{50} values were calculated from nuclear PAR staining intensity (10-12 images per condition; >800 cells) using GraphPad Prism. Error bars = SEM for 4 (PARG inhibitor) or 8 (veliparib) experiments. **** p<0.0001 (Brown-Forsythe and Welch ANOVA tests). **C**: TruHD cells were treated with 25 nM LMI070 for 24 hours prior to a 1-hour 10 μM PARG inhibitor pre-treatment followed by 100 mM $KBrO_3$ for 30 min in the presence of PARG inhibitor and analyzed as in Figure 1B. Results from 2 independent experiments (12 images per condition; >1000 cells) were analyzed by two-way ANOVA and corrected for multiple comparisons using Tukey's test. **D**: TruHD cells were treated with 25 nM LMI070 for 24 hours prior to 100 mM $KBrO_3$ for 30 min. γ-H2AX nuclear immunofluorescence intensity was quantified using CellProfiler, mean intensity recorded for each image (12 images per condition; >1000 cells), and values normalized to the control $KBrO_3$ response condition. Data from two independent experiments is shown. Results were analyzed by two-way ANOVA and corrected for multiple comparisons using Tukey's test (**** p<0.0001, *p<0.05).

Huntingtin interacts with PARylated proteins

Mutations associated with progressive cerebellar ataxia result in reduced expression of the scaffolding protein XRCC1, causing persistent unrepaired DNA damage and concomitant prolonged PARP1 activity [27]. Since PAR binding is important for the scaffolding function of XRCC1 in DNA repair complex formation [65], we sought to determine whether huntingtin also binds PAR.

We first interrogated the results of a mass spectrometry study identifying proteins that interact with huntingtin under conditions of oxidative stress (Table S1). The list of huntingtin interactors was compared to a compiled list of PARylated proteins from three independently generated datasets (**Fig S5**) [66–68]. As shown in **Figure 3**, 122 of the 298 (41%) huntingtin-interacting proteins were also found in a database of PARylated proteins. Fisher's test returned a significance of 2.1×10^{-81}. Thus, a significant proportion of huntingtin-interacting proteins are reported to be modified by PAR (Table S2).

We next asked whether huntingtin exists in complex with PARylated proteins in cells. As expected, PAR levels were increased in RPE1 cells treated with H_2O_2 (**Fig 3B**). Furthermore, PARylated proteins were enriched in huntingtin immunoprecipitates upon oxidative stress as shown by

western blot analysis. This is consistent with the high degree of overlap between datasets of huntingtin-interacting proteins and PARylated proteins.

To further investigate the relationship between huntingtin and PAR in human cells, we examined the subcellular localization of endogenous huntingtin upon manipulation of PAR production and degradation. While endogenous huntingtin localization in interphase cells was similar across conditions, we found that in mitotic cells treated with PARG inhibitor, huntingtin phosphorylated at residues S13 and S16 localized strongly to condensed mitotic chromosomes (**Fig 3C** and **Supplementary video 1**). This is similar to the staining pattern of PAR during mitosis [69,70]. In contrast, upon inhibition of PARP1/2 activity, huntingtin localized primarily to the mitotic spindle poles (**Fig S6**), as we and others have seen previously in untreated cells [71,72]. Together, these results suggest that huntingtin binds to PARylated proteins in human cells, and raises the possibility that huntingtin may directly bind PAR.

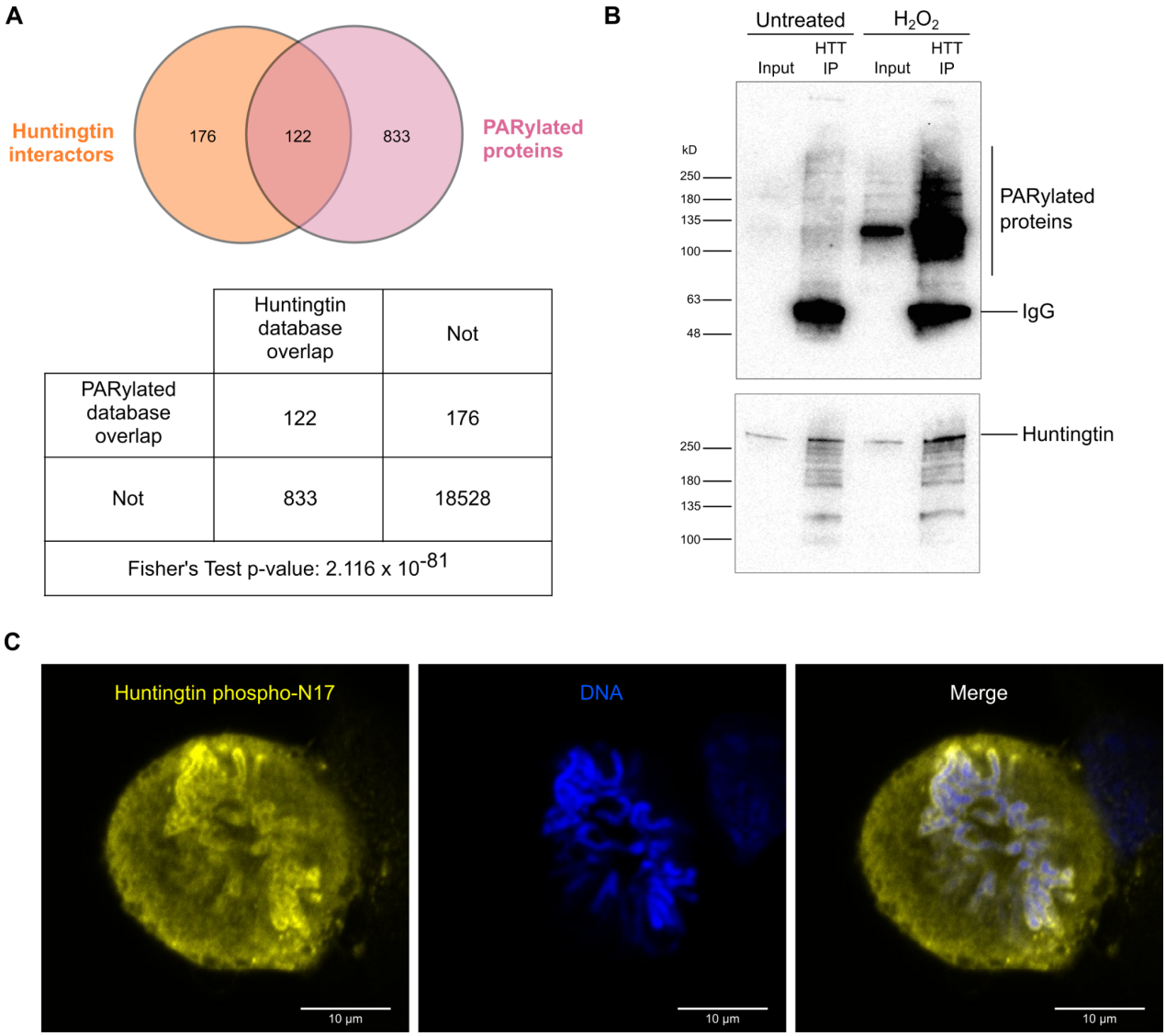

	Huntingtin database overlap	Not
PARylated database overlap	122	176
Not	833	18528
Fisher's Test p-value: 2.116×10^{-81}		

Figure 3: Huntingtin interacts with PARylated proteins

A: Top: degree of overlap between huntingtin interacting proteins and a list of PARylated proteins compiled from three independent studies. Bottom: Fisher's exact test for statistical significance. **B**: RPE1 cells were treated with 400 µM H_2O_2 in HBSS for 10 min and proteins crosslinked with 1% PFA prior to lysis. Huntingtin was immunoprecipitated with EPR5526 and associated proteins separated by SDS-PAGE and immunoblotted with the indicated antibodies. PARylated proteins of various sizes in the whole cell lysate (input) and anti-huntingtin immunoprecipitate (HTT IP) were detected with pan ADP-ribose detection reagent (MABE1016) followed by HRP-conjugated anti-rabbit secondary antibody. Rabbit IgG signal from the anti-huntingtin immunoprecipitating antibody (EPR5526) was visible upon incubation with secondary anti-rabbit antibody. Results representative of four experiments. **C**: RPE1 cells were treated with 10 µM PDD00017273 PARG inhibitor for 40 min prior to methanol fixation and immunofluorescence against huntingtin phosphorylated at residues S13 and S16 within the N17 domain and counterstaining with Hoechst. Image representative of all mitotic cells observed (n > 10 cells from two independent experiments).

Huntingtin contains a PAR-binding motif and directly binds PAR

We scanned the huntingtin sequence for potential PAR-binding motifs (PBMs) according to consensus sequences derived by Pleschke et al [73] and Gagne et al [66] and found 5 putative PBMs (**Fig 4A**). While huntingtin putative PBMs did not match the consensus with 100% similarity, their consensus fitting was comparable to those from previously validated PAR-binding proteins including DNA dependent protein kinase catalytic subunit (DNA-PK) [73] and 60 kD SS-A/Ro ribonucleoprotein [74].

To validate the bioinformatics results, we performed PAR overlay assays with peptides representing the putative PBMs (**Fig 4B**). PBM-3 displayed strong PAR-binding activity, which was ablated by mutation of the critical arginine residues. Multiple sequence alignment of human huntingtin and 9 orthologous species revealed a high degree of evolutionary conservation of PBM-3 and the surrounding sequences (**Fig 4C**). Mapping of this sequence on the cryo-EM structure of huntingtin [75] shows that PBM-3 is solvent accessible (**Fig 4D**), situated on the bridge domain at the interface of the N-HEAT domain with a surface area of ~890 $Å^2$. The motif spans a connecting loop region in this HEAT repeat in addition to a small section of each of the two flanking α-helices. The positively charged K1790, R1795 and R1796 residues are surface exposed in this model of the structure, indicating how they might interact with negatively charged PAR molecules.

We then asked whether the huntingtin PBM-3 bears resemblance to the PBM from the structurally similar [76] and functionally related [12] protein, ATM. Similar to ATM, the PAR-binding motif of huntingtin is a surface-exposed helix-turn-helix within a HEAT repeat (**Fig S7**). These results suggest that huntingtin PBM-3 is a *bona fide* PAR-binding motif, and that at least some of the interactions detected by immunoprecipitation and mass spectrometry (**Fig 3** and Table 1) could be direct.

A

ACCESSION	PROTEIN	RESIDUES	CONSENSUS ALIGNMENT							
			b	x	x	h	b	b	h	h
P78527	DNA-PK	2741-2748	L	M	Y	A	R	K	G	V
P55957	BID	153-160	L	L	L	A	K	K	V	A
O43684	BUB3	153-160	G	T	A	G	R	R	V	L
O76075	CAD	152-159	K	S	G	Y	L	R	Y	S
P10155	SS-A/Ro	146-152	R	-	A	L	R	K	A	I
Q00653	NFkB p100	179-185	K	-	E	L	K	K	V	M
P42858	HTT PBM-1	174-180	K	-	E	I	K	K	N	G
	HTT PBM-2	1530-1537	M	A	S	G	R	K	A	V
	HTT PBM-3	1790-1798	K S	G	M	F	R	R	I	T
	HTT PBM-x	1892-1899	R	E	I	V	R	R	G	A
	HTT PBM-4	2544-2550	R	-	F	G	R	K	L	S

B

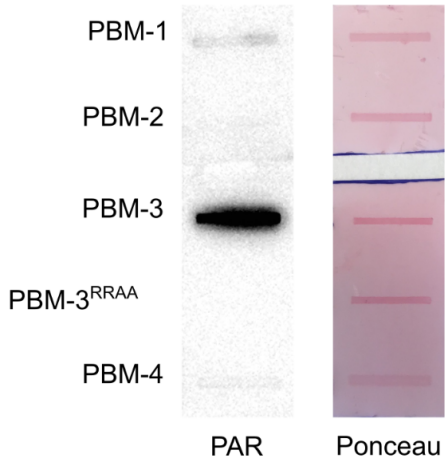

C

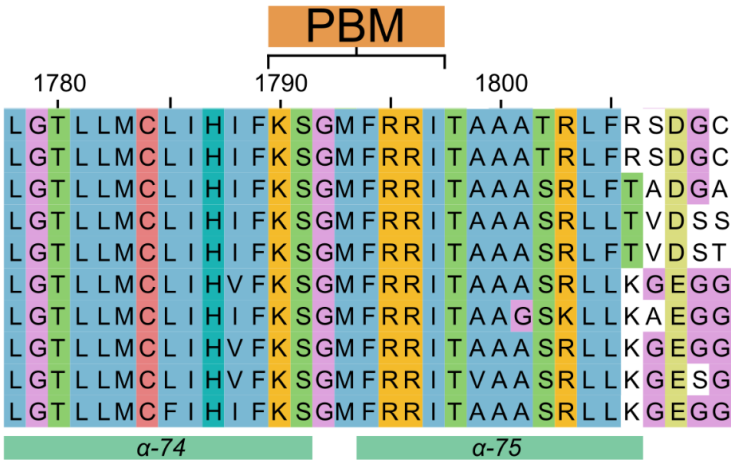

D

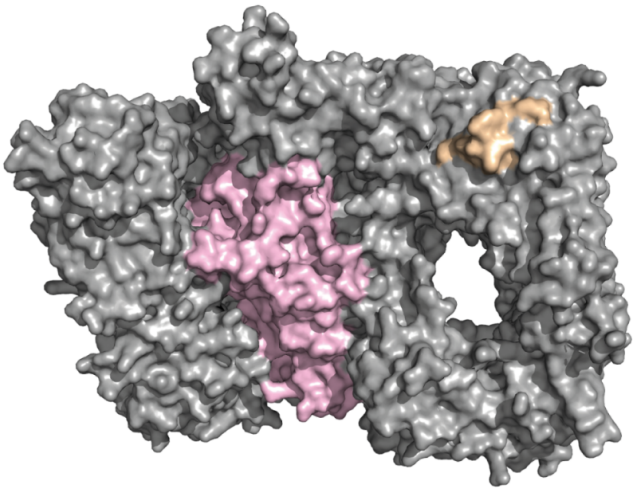

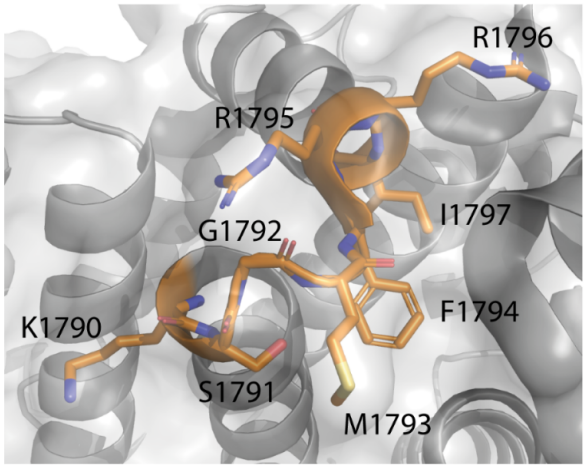

Figure 4: Huntingtin has a PAR-binding motif (PBM)
A: Known PBMs compared to putative PBMs in huntingtin. PBM-X is not solvent-accessible and was not analyzed further. b: basic, h: hydrophobic, x: any amino acid. Critical basic amino acids depicted in black boxes. **B**: Peptides were slot-blotted onto nitrocellulose then overlaid with 0.2 μM PAR polymer. After washing, anti-PAR western was performed with PAR detection reagent MABE1016. **C**: Multiple sequence alignment generated by Clustal Omega and visualized with JalView of huntingtin from human and orthologous species extracted from Ensembl. PAR binding motif (PBM) and flanking regions are shown with numbering reflecting human Q23 sequence and secondary structure based on 6X9O high resolution cryoEM model. **D**: Left: high resolution cryoEM model of huntingtin-HAP40 complex (PDB - 6X9O) shown in surface representation with huntingtin in gray, HAP40 in pink, and the PAR-binding motif in orange. Right: PAR-binding motif shown in stick representation in orange. Positively charged K1790, R1795 and R1796 residues are surface exposed.

To determine whether huntingtin physically interacts with PAR, we tested purified huntingtin protein and PAR linear polymer in a fluorescence polarization assay. As shown in **Fig 5A**, huntingtin binds long (26-mer) PAR chains, in preference to shorter (11-mer) substrates. This is similar to the substrate length specificity of other PAR binding proteins [77]. It should be noted that while these results support a direct interaction, the technical constraints of the experiment preclude saturation of the binding curve and therefore determination of binding kinetics and specificity. We next tested the PAR binding ability of different huntingtin subdomain constructs [78], and found that a construct comprising the N-HEAT and Bridge domains, which contains PBM-3, binds 26-mer PAR, while the C-HEAT domain (in complex with HAP40) does not (**Fig 5B**). We did not detect a significant difference in PAR binding between wild type and mutant huntingtin, nor upon deletion of the exon 1 domain in this assay (**Fig 5B**).

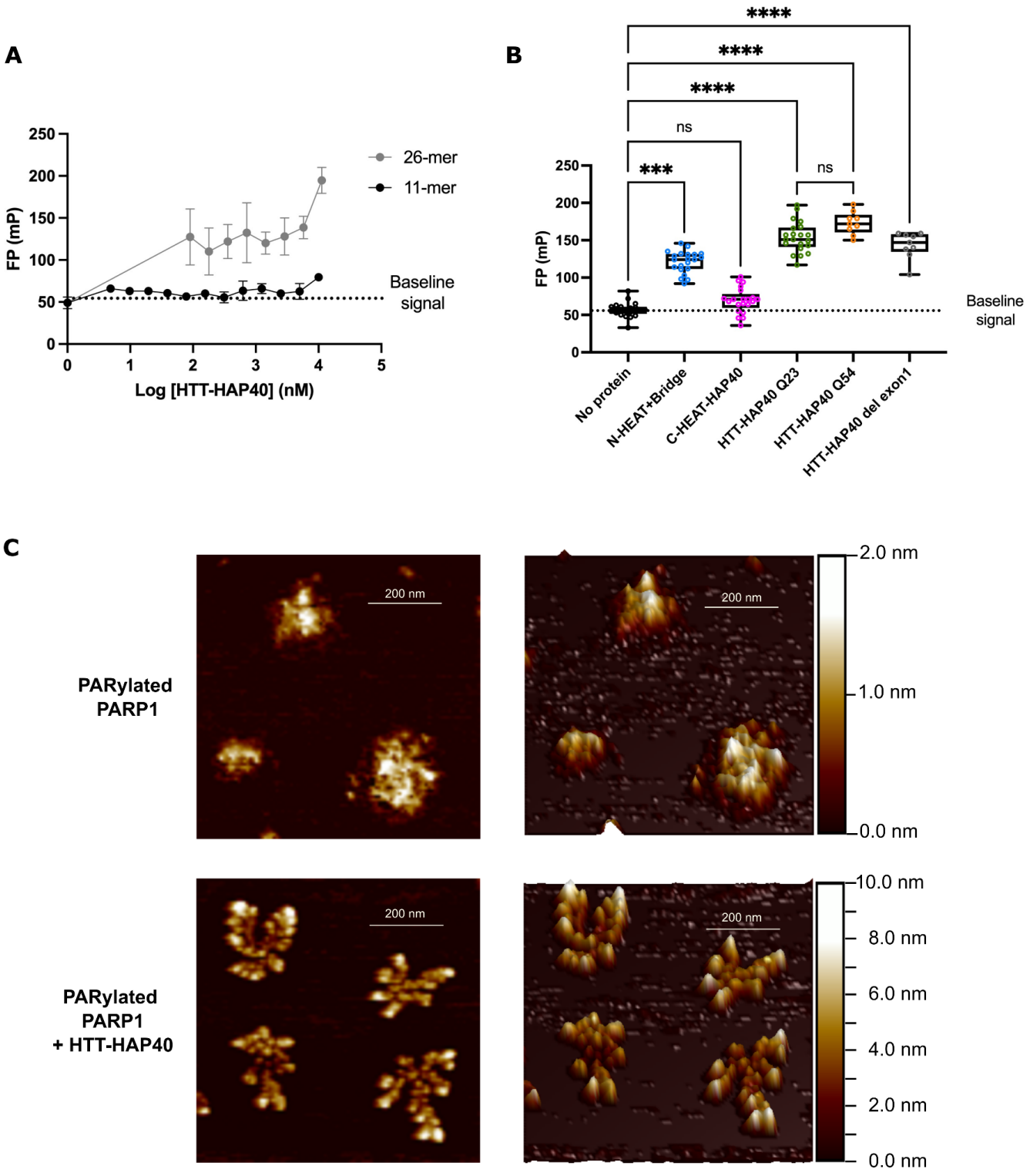
A
FP (mP)
250
200
150
100
50
0
0
1
2
3
4
5
Log [HTT-HAP40] (nM)
26-mer
11-mer
Baseline signal
B
****
****
****
ns
***
ns
FP (mP)
250
200
150
100
50
0
Baseline signal
No protein
N-HEAT+Bridge
C-HEAT-HAP40
HTT-HAP40 Q23
HTT-HAP40 Q54
HTT-HAP40 del exon1
C
PARylated PARP1
PARylated PARP1 + HTT-HAP40
200 nm
2.0 nm
1.0 nm
0.0 nm
10.0 nm
8.0 nm
6.0 nm
4.0 nm
2.0 nm
0.0 nm

Figure 5: Huntingtin directly binds PAR
A: Fluorescence polarization assays using FAM-labeled 11-mer or 26-mer PAR and purified HTT-HAP40 Q23. Results for 2 experiments are shown. Error bars = SD. **B**: Fluorescence polarization assays using FAM-labeled 26-mer PAR and 10 μM of the indicated subdomains of huntingtin. Reactions were carried out with 3-4 intra-assay replicates. Results for 3 experiments were analyzed by one-way ANOVA and corrected for multiple comparisons by Kruskal-Wallis test (***$p<0.0005$, ****$p<0.0001$). **C**: Recombinant HTT-HAP40 (0.2 nM) was added to PARP1 activity assays (1 nM recombinant PARP1, 50 mM Tris HCl pH 7.75, 50 mM NaCl, 5 mM NAD^+, 30 ng/μL sonicated salmon sperm DNA incubated at 30°C for 1-2 hours). Reactions were deposited on mica and visualized by atomic force microscopy. 2D (left) and 3D (right) images are shown with corresponding colour scale for PARylated PARP1 (2.0 nm) or PARylated PARP1 with HTT-HAP40 (10.0 nm).

In order to test whether huntingtin may bind PAR chains of various sizes, we included purified huntingtin protein in *in vitro* PARP1 reactions, and visualized the reactions by atomic force microscopy. In the absence of huntingtin, we observed auto-PARylated PARP1 structures consistent with previous reports [79–81] (**Fig 5C**). In contrast, the presence of huntingtin protein in the PARP1 reactions resulted in large rosette structures consistent with huntingtin protein bound to PAR chains (**Fig 5C**).

Taken together, these results suggest that huntingtin binds directly to PAR chains *in vitro*, which may account for its interaction with PARylated proteins in cells. Future studies are needed to determine whether mutant huntingtin PAR binding is responsible for the dysregulated PAR signaling we have observed in HD CSF and fibroblasts.

Discussion

The huntingtin protein is a large scaffold that participates in numerous cellular processes [82]. We have previously defined a role for huntingtin in the response to oxidative DNA damage [12], and characterized the nuclear localization signal [83] and nuclear export signals [84,85] regulating its translocation from the ER to the nucleus [71,86,87]. Here, we define an evolutionarily conserved

PAR-binding motif and show that huntingtin interacts with PARylated proteins. In cells from HD patients, PARP1/2 activity is diminished, which may contribute to the reduced levels of PAR we observed in the CSF from HD patients.

The elevated PAR levels we detected in cells from HD patients in the context of PARG inhibition are consistent with the elevated levels of DNA damage seen in HD models and tissues [11–18]. While many possible mechanisms could contribute to this, we have previously hypothesized that aberrant mutant huntingtin function in the repair of DNA plays a role [29,88]. Our identification and characterization of a PBM within huntingtin raises the possibility that huntingtin PAR interactions may be a factor in this feature of HD pathology. Huntingtin PAR binding appears to result in a different PAR chain morphology, which could scaffold a unique set of DNA repair factors. The ability to bind PAR is preferentially on longer chains, indicating that this binding is downstream of early PARP1 recognition and activation on DNA damage. This is consistent with our previous study in which we demonstrated that huntingtin recruitment to DNA was downstream of ATM kinase activity [12].

The decreased PAR levels we detected in the CSF from HD patients, an anomaly by comparison to similar studies in different neurodegenerative diseases [27,45–47], nonetheless reflect dysregulated PAR signaling in HD. While PAR levels did not correlate with disease measures, the robust reduction in PAR, even in premanifest patients, provides clinically relevant evidence for a role of PAR signaling dysregulation in the early stages of disease. The important caveat is that CSF PAR is not intraneuronal PAR, and the clinical data from CSF may only indicate that there is an abnormal PAR dynamic process, hence an impaired ability to repair DNA, as seen clinically by others as early as premanifest HD [13,14]. By use of the LMI070 splice modulator drug, we could restore PAR levels and DNA damage measured by γH2AX by reducing huntingtin protein levels, but we note this was achieved with only 30% lowering, suggesting current clinical goals of a 50% reduction in huntingtin protein may not be necessary, and toxicity issues seen to date in HD lowering clinical trials may be avoided [89].

Dysregulation of PAR signaling has now been linked to multiple neurodegenerative diseases. A common theme among these disorders is the hyperactivation of PARP1 in response to oxidative damage. This may also be the case in HD, as evidenced by strong PARP1 expression in the neurons

and glia of caudate nucleus from affected HD patients [50], and by the beneficial effect of PARP1 inhibition in the R6/2 mouse model [48,49]. In contrast, we detected lower PAR levels in HD patient CSF and reduced PARP1/2 activity in fibroblasts from HD patients. The R6/2 mouse model, which expresses only the first 81 amino acids, or only 2.6% of huntingtin, may not reflect the normal function of full-length huntingtin in PAR biology, and therefore exhibit different phenotypes than patient-derived materials. In addition, PAR levels in those studies were not measured, so we do not know whether PAR levels were elevated in this strain of HD mice, nor whether they were decreased after treatment with PARP1 inhibitor. The anomalous PAR dysregulation in HD compared to other neurodegenerative diseases may parallel the paradoxical PARP inhibitor and PARG inhibitor cancer treatment options [90], which show that tipping the balance in either direction is detrimental to cancer cells. Static measurements of hypo- and hyper-PARylation may not reflect the dynamic nature of PAR metabolism, but may instead act as the “canary in the coal mine” reporting on PAR signaling dysregulation in HD.

It is interesting to speculate that dysregulation of PAR signaling in HD may have beneficial secondary consequences, such as the reduced cancer rates seen in CAG expansion carriers [91], which could possibly be related to reduced PARP1/2 activity. This could in turn contribute to the apparent evolutionary advantage of longer CAG repeat lengths, which are not in equilibrium in human populations, but are subject to mutational bias towards expansion [92]. An interaction between HD and cancer via PARP1/2 activity may provide opportunity for the repurposing of currently available cancer drugs targeting this pathway. Future studies will look at different classes of FDA-approved PARP1 inhibitor drugs as some trap PARP1 on DNA, and some can cross the blood brain barrier while others cannot [51,52]. Interrogation of large banks of HD patient data [93] may make it possible to determine changes in disease progression associated with administration of such drugs, while the thriving development of new PARP and PARG inhibitors may hold promise for HD and neurodegenerative diseases at large.

Materials and Methods

Antibodies and reagents

All reagents were from MilliporeSigma unless otherwise stated. Veliparib (ABT-888) and LMI070 were from Selleckchem. PARG inhibitor (PDD00017273) was from AdipoGen Lifesciences. PAR (MABE1031) and pan ADP-ribose (MABE1016) detection reagents were from MilliporeSigma. Rabbit monoclonal anti-huntingtin antibody (EPR5526) was from Abcam. Mouse monoclonal anti-PARP1 (611039) was from BD Biosciences. Rabbit polyclonal anti-PARP2 (AB_2793328) was from Active Motif. Mouse polyclonal anti-PARG (ab169639) was from Abcam. Rabbit polyclonal anti-actin (20-33) was from MilliporeSigma. Rabbit monoclonal anti-vinculin (ab129002) was from Abcam. Rabbit monoclonal anti-γH2AX (ab81299) was from Abcam. Rabbit polyclonal antibodies against huntingtin N17 domain were described and validated previously [71]. Anti-rabbit IgG and anti-mouse IgG antibodies conjugated to HRP were from Abcam. Anti-rabbit IgG and anti-mouse IgG antibodies conjugated to Alexa Fluor 488 or 594 were from Invitrogen. Mica and specimen supports were from Ted Pella Inc.

Cell culture and treatments

TruHD cells [55] were cultured in MEM (Life Technologies #10370) with 15% fetal bovine serum (FBS; Life Technologies) and 1X GlutaMAX (Life Technologies #35050) and grown at 37°C with 5% CO_2 and 5-8% O_2. ST*Hdh* cells [94] were cultured in DMEM (Life Technologies #11995) with 10% FBS and grown at 33°C with 5% CO_2. RPE1 cells (American Type Culture Collection) were cultured in 1:1 DMEM/Nutrient Mixture F-12 (DMEM/F12; Life Technologies #11330) with 10% FBS and 0.01% hygromycin and grown at 37°C with 5% CO_2 and 5-8% O_2. Induction of DNA damage with H_2O_2 or $KBrO_3$ was done in Hank's balanced salt solution (HBSS) or phosphate-buffered saline (PBS), at the

concentrations and durations indicated in figure legends. 10 mM LMI070 stocks were prepared in DMSO and diluted in growth media for cell treatment.

STRIDE labeling of single- and double-strand breaks

Quantification of single- and double-strand breaks by STRIDE labeling [56] was performed by intoDNA (Kraków, Poland). Cells were seeded on cover glasses in 12-well plates at a density of 150,000 cells/well and left to rest for 24h. After fixation with 70% ethanol and storage at -20°C, sSTRIDE and dSTRIDE procedure was performed, followed by DAPI (Thermo Fisher) nucleus counterstaining, and CellMask Deep Red (Thermo Fisher, H32721) membrane staining. The coverslips with fixed cells were then mounted with Vectashield (Vectorlab) and stored at 4°C until imaging. Fields of view for imaging (at least 14 per sample) were chosen randomly over the surface of the coverslip and images collected as 3D confocal stacks. Quantitative analysis of collected data was performed using an in-house developed algorithm. The general analysis procedure consisted of recognition of cell nuclei based on DAPI staining, creation of a 3D mask for each recognized nuclei and its projection, creation of an approximated 3D mask of the cytoplasm and its projection, identification of STRIDE foci based on 3D local maxima of fluorescence, and quantification of the number of STRIDE foci within the 3D mask of the cell nucleus. All results generated by the algorithm underwent a thorough quality control. The accuracy of 3D nuclei masks, as well as STRIDE foci detection, were verified based on the images collected (raw data). In the case of unsatisfactory mask and/or foci recognition, the analysis was repeated using modified parameters.

Measurement of PAR levels in cells

Cells were seeded in 8-well ibiTreat µ-Slides (Ibidi) to ~95% confluence. After the indicated treatments, cells were fixed and permeabilized with cold methanol for 10 min at -20°C. Fixed cells were washed

with PBS, blocked with 10% FBS in PBS for 15 min and stained with either MABE1031 (PAR-binding) or MABE1016 (pan-ADP-ribose-binding) reagent diluted 1:500 in blocking buffer for 1 hour at room temperature. Following two PBS washes, cells were incubated with anti-rabbit secondary antibody diluted 1:500 in blocking buffer for 15 min at room temperature, washed with PBS and incubated with 0.2 ug/mL Hoechst in PBS for 5 min. Cells were imaged in PBS using the Nikon A1+ confocal system on a Nikon Eclipse Ti inverted microscope equipped with GaAsP detectors, using a PLAN APO 20×/0.75 dry objective. Nuclei were identified as primary objects in CellProfiler [95] using the Hoechst staining, then pixel intensity of the PAR staining within nuclei was calculated and the mean intensity recorded for each image. Ten to twelve images per well were captured, representing 800-1000 cells per experiment.

Human CSF samples

CSF samples were collected as part of the HD-CSF study, a prospective single-site study with standardized longitudinal collection of CSF, blood and phenotypic data (online protocol: 10.5522/04/11828448.v1). The cohort included manifest and premanifest HD mutation carriers as well as healthy controls who were age and gender matched to the entire HD mutation carrier group. In summary, lumbar punctures were performed after 12-hour fasting, in the early morning, and samples were processed within 30 minutes after the collection. Processed samples were aliquoted and stored at -80°C until shipment on dry ice for PAR quantification.

Measurement of PAR levels in CSF

PAR ELISA was performed as previously described [47]. CSF PAR values were assessed for normality and subsequently log transformed. We assessed potential confounders including age, gender, blood contamination and time in the freezer. There was an association between CSF PAR and storage time in

the freezer in healthy controls, therefore we included storage time as a covariate in all analyses. Group comparisons were assessed using multiple regression with post-hoc Wald tests.

Inhibitor dose response experiments

PARP1/2 and PARG activities were measured using the method described by James et al [62]. TruHD cells were grown in CellCarrier-96 Ultra Microplates (Perkin Elmer) and pre-treated with a dilution series of veliparib or PDD00017273 (8 points from 0-10 μM in duplicate) in fresh growth media for one hour. Cells were then treated for 30 min with 100 mM $KBrO_3$ dissolved in PBS containing Ca^{2+} and Mg^{2+} in the presence of the 8-point inhibitor dose range. Veliparib pre-treatment and $KBrO_3$ treatments included 5 μM PARG inhibitor for all conditions to enable visualization of the pan-ADP-ribose signal by MABE1016. After treatment, cells were fixed in cold methanol at -20°C for 10 min, washed with PBS, and blocked in 10% FBS in PBS for 15 min at room temperature. Indirect immunofluorescence against pan-ADP-ribose was performed using MABE1016 (1:750 dilution in blocking buffer) for 30 min at room temperature followed by Alexa Fluor donkey anti-rabbit-488 (1:1000 dilution in blocking buffer) for 15 min at room temperature. Nuclei were counterstained with 0.2 ug/mL Hoechst for 5 min and cells were imaged in PBS. Six fields per well were imaged using the 10× objective on the EVOS FL Auto 2 widefield microscope (1000-2000 cells per condition). Using CellProfiler [95], nuclei were identified by the Hoechst signal, pan-ADP-ribose signal intensity within nuclei was calculated, and the mean nuclear signal intensities for each field were averaged for each condition. Veliparib IC_{50} and PDD00017273 EC_{50} values were calculated using GraphPad Prism Version 9.4.1. Means were assessed by Brown-Forsythe and Welch ANOVA tests followed by Dunnett's T3 multiple comparisons test with individual variances computed for each comparison.

Immunofluorescence

To measure chromatin retention of PARP1, TruHD cells were grown in CellCarrier-96 Ultra Microplates (Perkin Elmer) and treated for 30 min with 100 mM $KBrO_3$ dissolved in PBS containing Ca^{2+} and Mg^{2+}. Soluble proteins were extracted with cold 0.2% Triton X-100 in PBS containing Ca^{2+} and Mg^{2+} for 2 min on ice prior to fixation and permeabilization with cold methanol for 10 min at -20°C. Fixed cells were washed with PBS, blocked with 10% FBS in PBS for 15 min and stained with mouse anti-PARP1 antibody (BD Biosciences) diluted 1:500 in blocking buffer for 1 hour at room temperature. Following two PBS washes, cells were incubated with anti-mouse secondary antibody diluted 1:500 in blocking buffer for 15 min at room temperature, washed with PBS and incubated with 0.2 ug/mL Hoechst in PBS for 5 min. Cells were imaged in PBS using the 10× objective on the EVOS FL Auto 2 widefield microscope (12 fields of view per condition; 2000-3000 cells).

For imaging of mitotic cells, RPE1 cells were fixed in cold methanol for 20 min at -20°C and incubated with blocking buffer (10% FBS in PBS) for 15 min at room temperature followed by anti-huntingtin phospho S13S16 antibody [71] (1:500 dilution in blocking buffer) for 45 min at room temperature, two washes with PBS, anti-rabbit secondary antibody (Alexa 594 or Alexa 488; 1:500 dilution in blocking buffer) for 20 min at room temperature and two washes with PBS. For co-staining of PARP1, cells were incubated with mouse anti-PARP1 antibody (BD Biosciences, 1:500 dilution in blocking buffer) for 1 hour at room temperature followed by two washes with PBS, anti-mouse secondary antibody (Alexa 488; 1:500 dilution in blocking buffer) for 20 min at room temperature and two washes with PBS. DNA was stained with 0.2 ug/mL Hoechst for 5 min at room temperature followed by a final PBS wash. Cell were imaged in PBS on a Nikon A1+ confocal system on a Nikon Eclipse Ti inverted microscope equipped with GaAsP detectors, using a PLAN APO 60×/1.40 oil objective. Image acquisition and Z-stack reconstruction was done with the Nikon NIS-Elements Advanced Research 64-bit acquisition software (Nikon).

Cell lysis and western analysis

For measurement of protein levels by western, cells were lysed using radioimmunoprecipitation assay buffer (50 mM Tris-HCl pH 8.0, 150 mM NaCl, 1% NP-40, 0.25% sodium deoxycholate, 1 mM EDTA) with protease and phosphatase inhibitors (Roche) and protein levels were measured with the Qubit Protein Broad Range (BR) Assay (ThermoFisher). Proteins were separated by SDS-PAGE using precast 4-20% gradient gels (Bio-Rad) and transferred to PVDF membrane (Millipore). Membranes were blocked in TBS-T (50 mM Tris-HCl, pH 7.5, 150 mM NaCl, 0.1% Tween-20) containing 5% skim milk powder for 1 hour and cut into sections to be probed with the indicated primary antibodies in the same buffer overnight at 4 °C. Membranes were washed six times with TBS-T then probed with horseradish peroxidase-conjugated secondary antibodies (Abcam) for 30 minutes at room temperature. After washing as above, membranes were incubated with enhanced chemiluminescence reagent (Millipore) and imaged with a MicroChemi chemiluminescence detector (DNR Bio-imaging Systems). The Gel Analyzer function on ImageJ was used to quantify protein signal.

Purification of huntingtin-interacting proteins

ST*Hdh*$^{Q7/Q7}$ mouse striatal precursor cells were treated with either HBSS, HBSS containing 60 µg/mL methyl methanesulfonate (MMS) for 20 min, or HBSS containing 100 µM H_2O_2 for 1 hour. Cells were harvested by trypsinization, then washed with ice cold PBS. Proteins were crosslinked with 1% paraformaldehyde for 10 min followed by washing with PBS. Lysates were prepared in cytoskeleton (CSK) buffer (10 mM PIPES, pH 6.8, 100 mM NaCl, 300 mM sucrose, 3 mM $MgCl_2$, 1 mM EGTA, 0.5% (v/v) Triton X-100) containing 1X protein and phosSTOP inhibitor cocktails (Roche) for 5 min on ice and cleared by centrifugation. Supernatants were pre-cleared with rabbit IgG and Protein A agarose beads

(MilliporeSigma) rotating for 30 min at 4°C. Pre-cleared products were collected and incubated in fresh Protein A agarose beads and anti-huntingtin EPR5526 (Abcam) for 2 hours rotating at 4°C. Immunoprecipitates were washed twice with CSK, twice with detergent-free CSK, and analyzed by mass spectrometry. For western blot analysis, RPE1 cells were treated with either HBSS or HBSS containing 400 μM H_2O_2 for 10 min and harvested as above.

Mass spectrometry and protein identification

Samples were trypsin-digested, desalted on C18 column, and LC-MS/MS performed on the Q Exactive HF-X mass spectrometer (SPARC BioCentre, Toronto, Canada). For database searching, tandem mass spectra were extracted by Proteome Discoverer. MS/MS samples were analyzed using Sequest (XCorr Only) (Thermo Fisher Scientific, San Jose, CA, USA; version IseNode in Proteome Discoverer 2.2.0.388) and X! Tandem (The GPM, thegpm.org; version CYCLONE (2010.12.01.1)). Sequest (XCorr Only) was set up to search Uniprot-Mus-Oct252017.fasta (25074 entries) assuming the digestion enzyme trypsin. X! Tandem was set up to search a reverse concatenated Uniprot-Mus-Oct252017 database (50196 entries) also assuming trypsin. Scaffold (version Scaffold_4.8.4, Proteome Software Inc., Portland, OR) was used to validate MS/MS based peptide and protein identifications. Peptide identifications were accepted if they could be established at greater than 95.0% probability. Peptide Probabilities from X! Tandem and Sequest (XCorr Only) were assigned by the Scaffold Local FDR algorithm or the Peptide Prophet algorithm [96] with Scaffold delta-mass correction. Protein identifications were accepted if they could be established at greater than 20.0% probability and contained at least 1 identified peptide. Protein probabilities were assigned by the Protein Prophet algorithm [97]. Proteins that contained similar peptides and could not be differentiated based on MS/MS analysis alone were grouped to satisfy the principles of parsimony.

PAR overlay assay

Peptides were ordered from Genscript and diluted to 0.5 mg/mL in PBS. PBM-1: LPRLQLELYKEIKKNGAPRSLR; PBM-2: KIIQLCDGIMASGRKAVTHAIPA; PBM-3: LLMCLIHFKSGMFRRITAAATRL; PBM-3 RR-AA: LLMCLIHFKSGMFAAITAAATRL; PBM-4: NKPLKALDTRFGRKLSIIRGIV. One microgram of each peptide was slot-blotted onto nitrocellulose membrane. Membranes were fixed in 2.5% glutaraldehyde/PBS for 30 min then washed with TBS-T (50 mM Tris-HCl, pH 7.5, 150 mM NaCl, 0.1% Tween-20), followed by incubation with 0.2 μM PAR polymer (Trevigen) in TBS-T for 30 min, three washes with excess TBS-T, and blocking with 5% milk in TBS-T for 15 min. PAR was detected using MABE1016 (1:1000 in TBS-T + 5% milk) and anti-rabbit-HRP (1:50000 in TBS-T + 5% milk). Membranes were then incubated with 0.5% Ponceau in 3% acetic acid for 10 min and washed in dH_2O.

Protein purification

Huntingtin and HAP40 constructs used in this study have been described previously [98] and are available through Addgene. Full-length PARP1 cDNA was subcloned into pFBOH-SBP-TEV-LIC and verified by sequencing. All proteins were produced in Sf9 culture as previously described [98]. Briefly, Sf9 cells infected with P3 recombinant baculovirus were grown until viability dropped to 80–85%, normally after ~72 h post-infection, at which point cell pellets were harvested by centrifugation. HTT samples were purified by FLAG-affinity chromatography and gel filtration as previously described [98]. For PARP1, cell pellets were lysed in buffer containing 20 mM HEPES pH 7.4, 300 mM NaCl, 1 mM TCEP, 2.5% glycerol spiked with 1X protease inhibitor mix and clarified by centrifugation before affinity purification using TALON resin (Cytiva). PARP1-bound resin was washed with lysis buffer supplemented with 5 mM imidazole and then eluted with lysis buffer containing 250 mM imidazole. PARP1 samples were further purified by gel filtration using S200 16/60 column (Cytiva) equilibrated in 20 mM HEPES pH 7.4, 150 mM NaCl, 1 mM TCEP, 2.5% glycerol. The peak corresponding to

monomeric PARP1 was pooled, concentrated ~10 mg/mL and aliquoted prior to flash-freezing in liquid nitrogen. All samples were assessed for purity by coomassie stained SDS-PAGE and were all shown to be >95% pure.

Fluorescence polarization

FAM-labeled 11-mer and 26-mer PAR were produced as described [99]. Fluorescence polarization reactions were carried out in 20 mM HEPES pH 7.4, 50 mM KCl, 2.5% glycerol, 1 mM TCEP, 2 mM $MgCl_2$, and 0.005% Tween-20 with a final concentration of 25 nM PAR substrate and 10 μM protein in a total reaction volume of 10 μL. Reactions were analysed using a Synergy H4 plate reader (Biotek) and data analysed using Graphpad Prism (version 9.4.1).

In vitro PARP1 reaction and atomic force microscopy

35 nM PARP1 was incubated with 5 μg/mL sonicated salmon sperm DNA (Abcam ab229278) in deposition buffer (12.5 mM HEPES pH 8, 12.5 mM KCl, 1 mM DTT) in the the presence of 100 μM NAD^+ and 10 mM $MgCl_2$ at 37°C for 30 min. Samples were diluted 10-fold in deposition buffer containing 3 mM $MgCl_2$ and 10 μL deposited on freshly cleaved mica for 5 min before rinsing with HPLC-grade water and drying under nitrogen stream. AFM images were captured in air on a Bruker Dimension iCon (Bruker, Santa-Barbara, CA, USA) in soft tapping mode with ScanAsyst-Air tip (Bruker). In this experiment, continuous force–distance curves were recorded at 256 x 256 pixels at line rate 0.996 Hz, and the tip was oscillated in the vertical direction with an amplitude of 100–300 nm and at low frequency (1–2 kHz). HTT-HAP40 particles alone or on the ends of PAR chains were selected using the mask function, and volumes calculated, with Image Metrics [100].

Statistical analysis

All data are represented as mean ± SEM with 3 independent experiments unless otherwise stated in the figure legends. Statistical analysis was performed using GraphPad Prism Version 9.4.1 and described for each experiment in figure legends. Differences among multiple means were assessed by ANOVA followed by Tukey's post hoc test. Non-normally distributed data were analyzed with nonparametric test (Mann-Whitney test). Assessments with $P < 0.05$ were considered significant. Eta squared values were used to determine effect size, with 0.01 representing a small effect, 0.06 representing a moderate effect, and 0.14 representing a large effect [101].

Acknowledgements

The authors gratefully acknowledge the participation of HD patients and families, without whom this work could not be completed. This research was supported by the Canadian Institutes of Health Research Project Grant (MOP-119391) and the Krembil Foundation (RT), the Huntington's Disease Society of America Berman Topper Career Development Fellowship and HD Human Biology Project (TM), Canadian Institutes of Health Research Project Grant (PJT180258 to SNA).

This work was also supported, in part, by a grant from the NIH R37 NS067525. T.M.D. is the Leonard and Madlyn Abramson Professor in Neurodegenerative Diseases.

EJW reports research grants from Medical Research Council (MR/M008592/1), CHDI Foundation, European Huntington's Disease Network, and F. Hoffmann-La Roche Ltd. The HD-CSF study was undertaken at the Leonard Wolfson Experimental Neurology Centre, University College London, supported by the National Institute for Health Research UCL Hospitals Biomedical Research Centre.

The Structural Genomics Consortium is a registered charity (no: 1097737) that receives funds from Bayer AG, Boehringer Ingelheim, Bristol Myers Squibb, Genentech, Genome Canada through Ontario Genomics Institute [OGI-196], EU/EFPIA/OICR/McGill/KTH/Diamond Innovative Medicines Initiative 2 Joint Undertaking [EUbOPEN grant 875510], Janssen, Merck KGaA (aka EMD in Canada and US), Pfizer and Takeda.

Disclosures

RT is a consultant to Novartis AG. EJW reports consultancy / advisory board memberships with Annexon, Remix Therapeutics, Hoffman La Roche Ltd, Ionis Pharmaceuticals, PTC Therapeutics, Takeda, Teitur Trophics, Triplet Therapeutics and Vico Therapeutics. All honoraria for these consultancies were paid through the offices of UCL Consultants Ltd., a wholly owned subsidiary of University College London. FBR is a Medpace UK Ltd employee and was a University College London employee during the conduct of this study. FBR has provided consultancy services to G.L.G. and F. Hoffmann-La Roche Ltd.

Author contributions

TM conceived the project, designed and conducted experiments, analyzed and interpreted data, supervised the project and wrote the manuscript. CBB, RJH, LMB, FBR, and MD designed and conducted experiments, analyzed and interpreted data and contributed to drafting and editing the manuscript. NB, TK, MMW, KN, MM, and MB conducted experiments and analyzed data. AKLL, SNA, EJW, TMD, VLD, CHA, and RT supervised the work, analyzed and interpreted data and contributed to drafting and editing the manuscript.

Materials and correspondence

All correspondence and requests for materials should be sent to TM (maiurit@mcmaster.ca) or RT (truantr@mcmaster.ca).

References

1. Lee J-M, Ramos EM, Lee J-H, Gillis T, Mysore JS, Hayden MR, et al. CAG repeat expansion in Huntington disease determines age at onset in a fully dominant fashion. Neurology. 2012;78: 690–695.

2. Genetic Modifiers of Huntington's Disease (GeM-HD) Consortium. CAG Repeat Not Polyglutamine Length Determines Timing of Huntington's Disease Onset. Cell. 2019;178: 887–900.e14.

3. Genetic Modifiers of Huntington's Disease (GeM-HD) Consortium. Identification of Genetic Factors that Modify Clinical Onset of Huntington's Disease. Cell. 2015;162: 516–526.

4. Djousse L, Knowlton B, Hayden M, Almqvist EW, Brinkman R, Ross C, et al. Interaction of normal and expanded CAG repeat sizes influences age at onset of Huntington disease. Am J Med Genet A. 2003;119: 279–282.

5. Wexler NS, Lorimer J, Porter J, Gomez F, Moskowitz C, Shackell E, et al. Venezuelan kindreds reveal that genetic and environmental factors modulate Huntington's disease age of onset. Proc Natl Acad Sci U S A. 2004;101: 3498–3503.

6. Bettencourt C, Hensman-Moss D, Flower M, Wiethoff S, Brice A, Goizet C, et al. DNA repair pathways underlie a common genetic mechanism modulating onset in polyglutamine diseases. Ann Neurol. 2016;79: 983–990.

7. Moss DJH, Pardiñas AF, Langbehn D, Lo K, Leavitt BR, Roos R, et al. Identification of genetic variants associated with Huntington's disease progression: a genome-wide association study. Lancet Neurol. 2017;16: 701–711.

8. Ciosi M, Maxwell A, Cumming SA, Hensman Moss DJ, Alshammari AM, Flower MD, et al. A genetic association study of glutamine-encoding DNA sequence structures, somatic CAG expansion, and DNA repair gene variants, with Huntington disease clinical outcomes. EBioMedicine. 2019;48: 568–580.

9. Goold R, Flower M, Moss DH, Medway C, Wood-Kaczmar A, Andre R, et al. FAN1 modifies Huntington's disease progression by stabilizing the expanded HTT CAG repeat. Hum Mol Genet. 2019;28: 650–661.

10. Flower M, Lomeikaite V, Ciosi M, Cumming S, Morales F, Lo K, et al. MSH3 modifies somatic

instability and disease severity in Huntington's and myotonic dystrophy type 1. Brain. 2019. doi:10.1093/brain/awz115

11. Lu X-H, Mattis VB, Wang N, Al-Ramahi I, van den Berg N, Fratantoni SA, et al. Targeting ATM ameliorates mutant Huntingtin toxicity in cell and animal models of Huntington's disease. Sci Transl Med. 2014;6: 268ra178.

12. Maiuri T, Mocle AJ, Hung CL, Xia J, van Roon-Mom WMC, Truant R. Huntingtin is a scaffolding protein in the ATM oxidative DNA damage response complex. Hum Mol Genet. 2017;26: 395–406.

13. Askeland G, Dosoudilova Z, Rodinova M, Klempir J, Liskova I, Kuśnierczyk A, et al. Increased nuclear DNA damage precedes mitochondrial dysfunction in peripheral blood mononuclear cells from Huntington's disease patients. Sci Rep. 2018;8: 9817.

14. Castaldo I, De Rosa M, Romano A, Zuchegna C, Squitieri F, Mechelli R, et al. DNA damage signatures in peripheral blood cells as biomarkers in prodromal huntington disease. Ann Neurol. 2019;85: 296–301.

15. Scudiero DA, Meyer SA, Clatterbuck BE, Tarone RE, Robbins JH. Hypersensitivity to N-methyl-N'-nitro-N-nitrosoguanidine in fibroblasts from patients with Huntington disease, familial dysautonomia, and other primary neuronal degenerations. Proc Natl Acad Sci U S A. 1981;78: 6451–6455.

16. Moshell AN, Tarone RE, Barrett SF, Robbins JH. Radiosensitivity in Huntington's disease: implications for pathogenesis and presymptomatic diagnosis. Lancet. 1980;1: 9–11.

17. Robison SH, Bradley WG. DNA damage and chronic neuronal degenerations. J Neurol Sci. 1984;64: 11–20.

18. Illuzzi J, Yerkes S, Parekh-Olmedo H, Kmiec EB. DNA breakage and induction of DNA damage response proteins precede the appearance of visible mutant huntingtin aggregates. J Neurosci Res. 2009;87: 733–747.

19. Lin X, Kapoor A, Gu Y, Chow MJ, Peng J, Zhao K, et al. Contributions of DNA Damage to Alzheimer's Disease. Int J Mol Sci. 2020;21. doi:10.3390/ijms21051666

20. Gonzalez-Hunt CP, Sanders LH. DNA damage and repair in Parkinson's disease: Recent advances and new opportunities. J Neurosci Res. 2020. doi:10.1002/jnr.24592

21. Massey TH, Jones L. The central role of DNA damage and repair in CAG repeat diseases. Dis Model Mech. 2018;11. doi:10.1242/dmm.031930

22. Yau WY, O'Connor E, Sullivan R, Akijian L, Wood NW. DNA repair in trinucleotide repeat ataxias. FEBS J. 2018;285: 3669–3682.

23. Penndorf D, Witte OW, Kretz A. DNA plasticity and damage in amyotrophic lateral sclerosis. Neural Regeneration Res. 2018;13: 173–180.

24. Moreira MC, Barbot C, Tachi N, Kozuka N, Uchida E, Gibson T, et al. The gene mutated in ataxia-ocular apraxia 1 encodes the new HIT/Zn-finger protein aprataxin. Nat Genet. 2001;29: 189–193.

25. Bras J, Alonso I, Barbot C, Costa MM, Darwent L, Orme T, et al. Mutations in PNKP cause recessive ataxia with oculomotor apraxia type 4. Am J Hum Genet. 2015;96: 474–479.

26. Takashima H, Boerkoel CF, John J, Saifi GM, Salih MAM, Armstrong D, et al. Mutation of TDP1 ,

encoding a topoisomerase I–dependent DNA damage repair enzyme, in spinocerebellar ataxia with axonal neuropathy. Nat Genet. 2002;32: 267–272.

27. Hoch NC, Hanzlikova H, Rulten SL, Tétreault M, Komulainen E, Ju L, et al. XRCC1 mutation is associated with PARP1 hyperactivation and cerebellar ataxia. Nature. 2017;541: 87–91.

28. Jaspers NG, Gatti RA, Baan C, Linssen PC, Bootsma D. Genetic complementation analysis of ataxia telangiectasia and Nijmegen breakage syndrome: a survey of 50 patients. Cytogenet Cell Genet. 1988;49: 259–263.

29. Maiuri T, Hung CLK, Suart C, Begeja N, Barba-Bazan C, Peng Y, et al. DNA Repair in Huntington's Disease and Spinocerebellar Ataxias: Somatic Instability and Alternative Hypotheses. J Huntingtons Dis. 2021;10: 165–173.

30. Gao R, Chakraborty A, Geater C, Pradhan S, Gordon KL, Snowden J, et al. Mutant huntingtin impairs PNKP and ATXN3, disrupting DNA repair and transcription. Elife. 2019;8. doi:10.7554/eLife.42988

31. Morozko EL, Smith-Geater C, Monteys AM, Pradhan S, Lim RG, Langfelder P, et al. PIAS1 modulates striatal transcription, DNA damage repair, and SUMOylation with relevance to Huntington's disease. Proc Natl Acad Sci U S A. 2021;118. doi:10.1073/pnas.2021836118

32. Suart C, Perez AM, Al-Ramahi I, Maiuri T, Botas J, Truant R. Spinocerebellar Ataxia Type 1 protein Ataxin-1 is signalled to DNA damage by Ataxia Telangiectasia Mutated kinase. 2019. p. 701953. doi:10.1101/701953

33. Narne P, Pandey V, Simhadri PK, Phanithi PB. Poly(ADP-ribose)polymerase-1 hyperactivation in neurodegenerative diseases: The death knell tolls for neurons. Semin Cell Dev Biol. 2017;63: 154–166.

34. Shieh WM, Amé JC, Wilson MV, Wang ZQ, Koh DW, Jacobson MK, et al. Poly(ADP-ribose) polymerase null mouse cells synthesize ADP-ribose polymers. J Biol Chem. 1998;273: 30069–30072.

35. Amé JC, Rolli V, Schreiber V, Niedergang C, Apiou F, Decker P, et al. PARP-2, A novel mammalian DNA damage-dependent poly(ADP-ribose) polymerase. J Biol Chem. 1999;274: 17860–17868.

36. Masson M, Niedergang C, Schreiber V, Muller S, Menissier-de Murcia J, de Murcia G. XRCC1 is specifically associated with poly(ADP-ribose) polymerase and negatively regulates its activity following DNA damage. Mol Cell Biol. 1998;18: 3563–3571.

37. El-Khamisy SF, Masutani M, Suzuki H, Caldecott KW. A requirement for PARP-1 for the assembly or stability of XRCC1 nuclear foci at sites of oxidative DNA damage. Nucleic Acids Res. 2003;31: 5526–5533.

38. Kamaletdinova T, Fanaei-Kahrani Z, Wang Z-Q. The Enigmatic Function of PARP1: From PARylation Activity to PAR Readers. Cells. 2019;8. doi:10.3390/cells8121625

39. Wei L, Nakajima S, Hsieh C-L, Kanno S, Masutani M, Levine AS, et al. Damage response of XRCC1 at sites of DNA single strand breaks is regulated by phosphorylation and ubiquitylation after degradation of poly(ADP-ribose). J Cell Sci. 2013;126: 4414–4423.

40. Maruta H, Matsumura N, Tanuma S-I. Role of (ADP-ribose)nCatabolism in DNA Repair. Biochem Biophys Res Commun. 1997;236: 265–269.

41. Oei SL, Ziegler M. ATP for the DNA Ligation Step in Base Excision Repair Is Generated from

Poly(ADP-ribose). J Biol Chem. 2000;275: 23234–23239.

42. Morales J, Li L, Fattah FJ, Dong Y, Bey EA, Patel M, et al. Review of poly (ADP-ribose) polymerase (PARP) mechanisms of action and rationale for targeting in cancer and other diseases. Crit Rev Eukaryot Gene Expr. 2014;24: 15–28.

43. Fatokun AA, Dawson VL, Dawson TM. Parthanatos: mitochondrial-linked mechanisms and therapeutic opportunities. Br J Pharmacol. 2014;171: 2000–2016.

44. Park H, Kam T-I, Dawson TM, Dawson VL. Poly (ADP-ribose) (PAR)-dependent cell death in neurodegenerative diseases. Int Rev Cell Mol Biol. 2020;353: 1–29.

45. Love S, Barber R, Wilcock GK. Increased poly(ADP-ribosyl)ation of nuclear proteins in Alzheimer's disease. Brain. 1999. pp. 247–253. doi:10.1093/brain/122.2.247

46. McGurk L, Mojsilovic-Petrovic J, Van Deerlin VM, Shorter J, Kalb RG, Lee VM, et al. Nuclear poly(ADP-ribose) activity is a therapeutic target in amyotrophic lateral sclerosis. Acta Neuropathologica Communications. 2018;6: 84.

47. Kam T-I, Mao X, Park H, Chou S-C, Karuppagounder SS, Umanah GE, et al. Poly(ADP-ribose) drives pathologic α-synuclein neurodegeneration in Parkinson's disease. Science. 2018;362. doi:10.1126/science.aat8407

48. Cardinale A, Paldino E, Giampà C, Bernardi G, Fusco FR. PARP-1 Inhibition Is Neuroprotective in the R6/2 Mouse Model of Huntington's Disease. PLoS One. 2015;10: e0134482.

49. Paldino E, Cardinale A, D'Angelo V, Sauve I, Giampà C, Fusco FR. Selective Sparing of Striatal Interneurons after Poly (ADP-Ribose) Polymerase 1 Inhibition in the R6/2 Mouse Model of Huntington's Disease. Front Neuroanat. 2017;11: 61.

50. Vis JC, Schipper E, de Boer-van Huizen RT, Verbeek MM, de Waal RMW, Wesseling P, et al. Expression pattern of apoptosis-related markers in Huntington's disease. Acta Neuropathologica. 2005. pp. 321–328. doi:10.1007/s00401-004-0957-5

51. Thapa K, Khan H, Sharma U, Grewal AK, Singh TG. Poly (ADP-ribose) polymerase-1 as a promising drug target for neurodegenerative diseases. Life Sci. 2021;267: 118975.

52. Berger NA, Besson VC, Boulares AH, Bürkle A, Chiarugi A, Clark RS, et al. Opportunities for the repurposing of PARP inhibitors for the therapy of non-oncological diseases. Br J Pharmacol. 2018;175: 192–222.

53. Palminha NM, Dos Santos Souza C, Griffin J, Liao C, Ferraiuolo L, El-Khamisy SF. Defective repair of topoisomerase I induced chromosomal damage in Huntington's disease. Cell Mol Life Sci. 2022;79: 1–21.

54. Ferlazzo ML, Sonzogni L, Granzotto A, Bodgi L, Lartin O, Devic C, et al. Mutations of the Huntington's disease protein impact on the ATM-dependent signaling and repair pathways of the radiation-induced DNA double-strand breaks: corrective effect of statins and bisphosphonates. Mol Neurobiol. 2014;49. doi:10.1007/s12035-013-8591-7

55. Hung CL-K, Maiuri T, Bowie LE, Gotesman R, Son S, Falcone M, et al. A Patient-Derived Cellular Model for Huntington's Disease Reveals Phenotypes at Clinically Relevant CAG Lengths. Mol Biol Cell. 2018; mbcE18090590.

56. Kordon MM, Zarębski M, Solarczyk K, Ma H, Pederson T, Dobrucki JW. STRIDE-a fluorescence method for direct, specific in situ detection of individual single- or double-strand DNA breaks in

fixed cells. Nucleic Acids Res. 2020;48: e14.

57. Haince J-F, McDonald D, Rodrigue A, Déry U, Masson J-Y, Hendzel MJ, et al. PARP1-dependent kinetics of recruitment of MRE11 and NBS1 proteins to multiple DNA damage sites. J Biol Chem. 2008;283: 1197–1208.

58. Caron M-C, Sharma AK, O'Sullivan J, Myler LR, Ferreira MT, Rodrigue A, et al. Poly(ADP-ribose) polymerase-1 antagonizes DNA resection at double-strand breaks. Nat Commun. 2019;10: 1–16.

59. Couto CA-M, Wang H-Y, Green JCA, Kiely R, Siddaway R, Borer C, et al. PARP regulates nonhomologous end joining through retention of Ku at double-strand breaks. J Cell Biol. 2011;194: 367–375.

60. Byrne LM, Rodrigues FB, Johnson EB, Wijeratne PA, De Vita E, Alexander DC, et al. Evaluation of mutant huntingtin and neurofilament proteins as potential markers in Huntington's disease. Sci Transl Med. 2018;10. doi:10.1126/scitranslmed.aat7108

61. Rodrigues FB, Byrne LM, Tortelli R, Johnson EB, Wijeratne PA, Arridge M, et al. Mutant huntingtin and neurofilament light have distinct longitudinal dynamics in Huntington's disease. Sci Transl Med. 2020;12. doi:10.1126/scitranslmed.abc2888

62. James DI, Durant S, Eckersley K, Fairweather E, Griffiths LA, Hamilton N, et al. An assay to measure poly(ADP ribose) glycohydrolase (PARG) activity in cells. F1000Res. 2016;5: 736.

63. Keller CG, Shin Y, Monteys AM, Renaud N, Beibel M, Teider N, et al. An orally available, brain penetrant, small molecule lowers huntingtin levels by enhancing pseudoexon inclusion. Nat Commun. 2022;13: 1–11.

64. Monteys AM, Hundley AA, Ranum PT, Tecedor L, Muehlmatt A, Lim E, et al. Regulated control of gene therapies by drug-induced splicing. Nature. 2021;596: 291–295.

65. Caldecott KW. XRCC1 protein; Form and function. DNA Repair . 2019;81. doi:10.1016/j.dnarep.2019.102664

66. Gagné J-P, Isabelle M, Lo KS, Bourassa S, Hendzel MJ, Dawson VL, et al. Proteome-wide identification of poly(ADP-ribose) binding proteins and poly(ADP-ribose)-associated protein complexes. Nucleic Acids Res. 2008;36: 6959–6976.

67. Zhang Y, Wang J, Ding M, Yu Y. Site-specific characterization of the Asp- and Glu-ADP-ribosylated proteome. Nat Methods. 2013;10: 981–984.

68. Jungmichel S, Rosenthal F, Altmeyer M, Lukas J, Hottiger MO, Nielsen ML. Proteome-wide identification of poly(ADP-Ribosyl)ation targets in different genotoxic stress responses. Mol Cell. 2013;52: 272–285.

69. Kanai Y. Overview on poly(ADP-ribose) immuno-biomedicine and future prospects. Proc Jpn Acad Ser B Phys Biol Sci. 2016;92: 222.

70. Kanai Y, Tanuma S, Sugimura T. Immunofluorescent staining of poly(ADP-ribose) in situ in HeLa cell chromosomes in the M phase. Proc Natl Acad Sci U S A. 1981;78: 2801.

71. Atwal RS, Desmond CR, Caron N, Maiuri T, Xia J, Sipione S, et al. Kinase inhibitors modulate huntingtin cell localization and toxicity. Nat Chem Biol. 2011;7: 453–460.

72. Godin JD, Colombo K, Molina-Calavita M, Keryer G, Zala D, Charrin BC, et al. Huntingtin is required for mitotic spindle orientation and mammalian neurogenesis. Neuron. 2010;67: 392–406.

73. Pleschke JM, Kleczkowska HE, Strohm M, Althaus FR. Poly (ADP-ribose) binds to specific domains in DNA damage checkpoint proteins. J Biol Chem. 2000;275: 40974–40980.

74. Gagné J-P, Hunter JM, Labrecque B, Chabot B, Poirier GG. A proteomic approach to the identification of heterogeneous nuclear ribonucleoproteins as a new family of poly(ADP-ribose)-binding proteins. Biochem J. 2003;371: 331–340.

75. Harding RJ, Deme JC, Hevler JF, Tamara S, Lemak A, Cantle JP, et al. Huntingtin structure is orchestrated by HAP40 and shows a polyglutamine expansion-specific interaction with exon 1. Communications Biology. 2021;4: 1–16.

76. Xiao J, Liu M, Qi Y, Chaban Y, Gao C, Pan B, et al. Structural insights into the activation of ATM kinase. Cell Res. 2019;29: 683–685.

77. Reber JM, Mangerich A. Why structure and chain length matter: on the biological significance underlying the structural heterogeneity of poly(ADP-ribose). Nucleic Acids Res. 2021;49: 8432–8448.

78. Alteen MG, Deme JC, Alvarez CP, Loppnau P, Hutchinson A, Seitova A, et al. Expanding the Huntingtons disease research toolbox; validated huntingtin subdomain constructs for biochemical and structural investigation of the huntingtin protein. bioRxiv. 2022. p. 2022.11.21.516512. doi:10.1101/2022.11.21.516512

79. Naumenko KN, Sukhanova MV, Hamon L, Kurgina TA, Anarbaev RO, Mangerich A, et al. The C-Terminal Domain of Y-Box Binding Protein 1 Exhibits Structure-Specific Binding to Poly(ADP-Ribose), Which Regulates PARP1 Activity. Frontiers in Cell and Developmental Biology. 2022;10. doi:10.3389/fcell.2022.831741

80. Sukhanova MV, Abrakhi S, Joshi V, Pastre D, Kutuzov MM, Anarbaev RO, et al. Single molecule detection of PARP1 and PARP2 interaction with DNA strand breaks and their poly(ADP-ribosyl)ation using high-resolution AFM imaging. Nucleic Acids Res. 2015;44: e60–e60.

81. Naumenko KN, Sukhanova MV, Hamon L, Kurgina TA, Alemasova EE, Kutuzov MM, et al. Regulation of Poly(ADP-Ribose) Polymerase 1 Activity by Y-Box-Binding Protein 1. Biomolecules. 2020;10: 1325.

82. Saudou F, Humbert S. The Biology of Huntingtin. Neuron. 2016;89: 910–926.

83. Desmond CR, Atwal RS, Xia J, Truant R. Identification of a karyopherin β1/β2 proline-tyrosine nuclear localization signal in huntingtin protein. J Biol Chem. 2012;287: 39626–39633.

84. Xia J, Lee DH, Taylor J, Vandelft M, Truant R. Huntingtin contains a highly conserved nuclear export signal. Hum Mol Genet. 2003;12: 1393–1403.

85. Maiuri T, Woloshansky T, Xia J, Truant R. The huntingtin N17 domain is a multifunctional CRM1 and Ran-dependent nuclear and cilial export signal. Hum Mol Genet. 2013;22: 1383–1394.

86. Atwal RS, Xia J, Pinchev D, Taylor J, Epand RM, Truant R. Huntingtin has a membrane association signal that can modulate huntingtin aggregation, nuclear entry and toxicity. Hum Mol Genet. 2007;16: 2600–2615.

87. DiGiovanni LF, Mocle AJ, Xia J, Truant R. Huntingtin N17 domain is a reactive oxygen species sensor regulating huntingtin phosphorylation and localization. Hum Mol Genet. 2016. doi:10.1093/hmg/ddw234

88. Maiuri T, Bowie LE, Truant R. DNA Repair Signaling of Huntingtin: The Next Link Between

Late-Onset Neurodegenerative Disease and Oxidative DNA Damage. DNA Cell Biol. 2019;38: 1–6.

89. Tabrizi SJ, Estevez-Fraga C, van Roon-Mom WMC, Flower MD, Scahill RI, Wild EJ, et al. Potential disease-modifying therapies for Huntington's disease: lessons learned and future opportunities. Lancet Neurol. 2022;21: 645–658.

90. Slade D. PARP and PARG inhibitors in cancer treatment. Genes Dev. 2020;34: 360–394.

91. McNulty P, Pilcher R, Ramesh R, Necuiniate R, Hughes A, Farewell D, et al. Reduced Cancer Incidence in Huntington's Disease: Analysis in the Registry Study. J Huntingtons Dis. 2018;7: 209–222.

92. Rubinsztein DC, Amos W, Leggo J, Goodburn S, Ramesar RS, Old J, et al. Mutational bias provides a model for the evolution of Huntington's disease and predicts a general increase in disease prevalence. Nat Genet. 1994;7: 525–530.

93. Landwehrmeyer GB, Fitzer-Attas CJ, Giuliano JD, Gonçalves N, Anderson KE, Cardoso F, et al. Data Analytics from Enroll-HD, a Global Clinical Research Platform for Huntington's Disease. Mov Disord Clin Pract. 2017;4: 212–224.

94. Trettel F, Rigamonti D, Hilditch-Maguire P, Wheeler VC, Sharp AH, Persichetti F, et al. Dominant phenotypes produced by the HD mutation in STHdh(Q111) striatal cells. Hum Mol Genet. 2000;9: 2799–2809.

95. Carpenter AE, Jones TR, Lamprecht MR, Clarke C, Kang IH, Friman O, et al. CellProfiler: image analysis software for identifying and quantifying cell phenotypes. Genome Biol. 2006;7: R100.

96. Keller A, Nesvizhskii AI, Kolker E, Aebersold R. Empirical statistical model to estimate the accuracy of peptide identifications made by MS/MS and database search. Anal Chem. 2002;74: 5383–5392.

97. Nesvizhskii AI, Keller A, Kolker E, Aebersold R. A statistical model for identifying proteins by tandem mass spectrometry. Anal Chem. 2003;75: 4646–4658.

98. Harding RJ, Loppnau P, Ackloo S, Lemak A, Hutchinson A, Hunt B, et al. Design and characterization of mutant and wildtype huntingtin proteins produced from a toolkit of scalable eukaryotic expression systems. J Biol Chem. 2019;294: 6986–7001.

99. Ando Y, Elkayam E, McPherson RL, Dasovich M, Cheng S-J, Voorneveld J, et al. ELTA: Enzymatic Labeling of Terminal ADP-Ribose. Mol Cell. 2019;73: 845–856.e5.

100. Andres SN, Li ZM, Erie DA, Williams RS. Ctp1 protein-DNA filaments promote DNA bridging and DNA double-strand break repair. J Biol Chem. 2019;294: 3312–3320.

101. Pallant J. SPSS survival manual: A step by step guide to data analysis using IBM SPSS. [cited 11 Oct 2022]. doi:10.4324/9781003117452/spss-survival-manual-julie-pallant